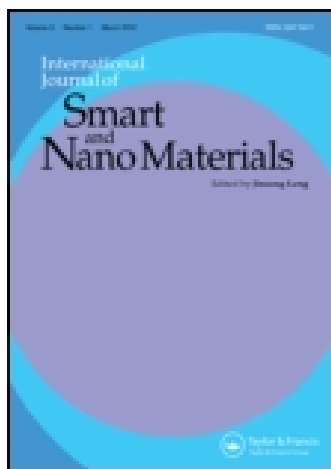


This article was downloaded by: [Beijing Institute of Technology]

On: 22 April 2015, At: 02:52

Publisher: Taylor & Francis

Informa Ltd Registered in England and Wales Registered Number: 1072954 Registered office: Mortimer House, 37-41 Mortimer Street, London W1T 3JH, UK



International Journal of Smart and Nano Materials

Publication details, including instructions for authors and subscription information:

<http://www.tandfonline.com/loi/tsnm20>

Microstructural designs of plate-type elastic metamaterial and their potential applications: a review

R. Zhu^a, X.N. Liu^b, G.K. Hu^b, F.G. Yuan^a & G.L. Huang^c

^a Department of Mechanical and Aerospace Engineering, North Carolina State University, Raleigh, NC 27695, USA

^b School of Aerospace Engineering, Beijing Institute of Technology, Beijing 100081, People's Republic of China

^c Department of Mechanical and Aerospace Engineering, University of Missouri, Columbia, MO 65211, USA

Published online: 24 Mar 2015.



CrossMark

[Click for updates](#)

To cite this article: R. Zhu, X.N. Liu, G.K. Hu, F.G. Yuan & G.L. Huang (2015) Microstructural designs of plate-type elastic metamaterial and their potential applications: a review, International Journal of Smart and Nano Materials, 6:1, 14-40, DOI: [10.1080/19475411.2015.1025249](https://doi.org/10.1080/19475411.2015.1025249)

To link to this article: <http://dx.doi.org/10.1080/19475411.2015.1025249>

PLEASE SCROLL DOWN FOR ARTICLE

Taylor & Francis makes every effort to ensure the accuracy of all the information (the "Content") contained in the publications on our platform. Taylor & Francis, our agents, and our licensors make no representations or warranties whatsoever as to the accuracy, completeness, or suitability for any purpose of the Content. Versions of published Taylor & Francis and Routledge Open articles and Taylor & Francis and Routledge Open Select articles posted to institutional or subject repositories or any other third-party website are without warranty from Taylor & Francis of any kind, either expressed or implied, including, but not limited to, warranties of merchantability, fitness for a particular purpose, or non-infringement. Any opinions and views expressed in this article are the opinions and views of the authors, and are not the views of or endorsed by Taylor & Francis. The accuracy of the Content should not be relied upon and should be independently verified with primary sources of information. Taylor & Francis shall not be liable for any losses, actions, claims, proceedings, demands, costs, expenses, damages, and other liabilities whatsoever or howsoever caused arising directly or indirectly in connection with, in relation to or arising out of the use of the Content.

This article may be used for research, teaching, and private study purposes. Terms & Conditions of access and use can be found at <http://www.tandfonline.com/page/terms-and-conditions>

It is essential that you check the license status of any given Open and Open Select article to confirm conditions of access and use.

Microstructural designs of plate-type elastic metamaterial and their potential applications: a review

R. Zhu^{a*}, X.N. Liu^b, G.K. Hu^b, F.G. Yuan^a and G.L. Huang^{c*}

^aDepartment of Mechanical and Aerospace Engineering, North Carolina State University, Raleigh, NC 27695, USA; ^bSchool of Aerospace Engineering, Beijing Institute of Technology, Beijing 100081, People's Republic of China; ^cDepartment of Mechanical and Aerospace Engineering, University of Missouri, Columbia, MO 65211, USA

(Received 7 February 2015; final version received 27 February 2015)

Elastic metamaterials are of growing interest due to their unique effective properties and wave manipulation abilities. Unlike phononic crystals based on the Bragg scattering mechanism, elastic metamaterials (EMMs) are based on the locally resonant (LR) mechanism and can fully control elastic waves at a subwavelength scale. Microstructural designs of EMMs in plate-like structures have attracted a great deal of attention. In this paper, the recent advances in the microstructural designs of LR-based EMM plates are reviewed. Their potential applications in the fields of low frequency guided wave attenuation, wave manipulation and energy trapping at a subwavelength scale, and structural health monitoring are discussed.

Keywords: metamaterial; composite; structural dynamics; nondestructive evaluation; structural health monitoring

1. Introduction

The research on metamaterials has grasped a lot of attentions recently. With artificially designed microstructures, metamaterial has the ability to achieve bizarre but very useful dynamic material properties. Initially, the strangeness of metamaterial was discovered when researchers investigated its effective electromagnetic (EM) properties at certain frequency ranges where the EM metamaterial behaves as if it has negative permittivity [1] and/or negative permeability [2]. Later on, similar unnatural phenomena were found in acoustic metamaterials which have negative mass density (NMD) [3] and/or negative bulk modulus (NBM) [4]. Anisotropic mass density was also achieved in non-resonant acoustic metamaterials containing fluid components [5,6,7]. Unlike the essential similarity between the governing equations in EM metamaterials and those in acoustic metamaterials, applying the concept of metamaterial in solids is more complex [8]. This is mainly due to the inherent coupling between longitudinal and shear wave modes and wave mode conversion. However, driven by the curiosity as well as the promising applications in mechanical and aerospace engineering, researchers have become more and more interested in the abnormal effective material properties of elastic metamaterials (EMMs). Many EMM-based devices have been proposed for promising applications with elastic wave controls and manipulations such as: elastic wave flat-lens focusing [9], EMM waveguides [10], EMM cloaking [11], and sub-wavelength imaging [12].

*Corresponding authors. Email: rzhu2@ncsu.edu (R. Zhu); HuangG@missouri.edu (G.L. Huang)

One of the biggest advantages of EMM over other wave-control structures, such as phononic crystals (PCs), is that the size of the metamaterial can be very small even in the low frequency range. Like photonic crystals, PCs have periodic structures with spatially modulated mechanical properties and therefore, can block or redirect acoustic/elastic waves based on the Bragg scattering mechanism. However, a reliance on Bragg scattering makes PC unsuited for either wave manipulation or vibration isolation at low frequency range due to the long wavelength necessitating impractically huge structures. By introducing the specially designed locally resonant (LR) microstructures into the building block of a PC, bandgap can be created at an extremely low-frequency range [13] where the wavelength becomes much larger than the size of the microstructure inside the EMM. The advantage of the subwavelength-scale LR microstructure is twofold: LR EMM based devices can be made small enough to be easily implanted into the engineering structures without sacrificing their lightness and compactness, and with an inhomogeneity scale that is much smaller than the wavelength of interest, EMM can be treated as a homogeneous medium with effective dynamic material properties.

With specially designed LR microstructures, unique negative effective material properties can be achieved in solid EMMs such as NMD, NBM and negative shear modulus. The frequency ranges where EMM demonstrates negative material property are found to be overlapped with the bandgaps that could, therefore, be easily tuned by changing the effective material properties through proper subwavelength-scale microstructural design. To understand the relationships between the negative effective material properties and the bandgaps in EMM, Milton and Willis [14] employed a simple one-dimensional (1D) mass-spring model to produce NMD. Yao *et al.* [15] experimentally examined the model in the low frequency regime, NMD was confirmed at the bandgap region of a finite periodic system composed of mass-spring units. For continuum media, Wang *et al.* [16] investigated the propagation of longitudinal and transverse elastic waves in a 1D infinite periodically layered system and the difference between the Bragg scattering mechanism in PC and the LR mechanism in EMM are discussed. Zhu *et al.* [17] proposed a 1D multilayered EMM design to achieve multiple bandgaps based on NMD retrieved from the theoretical reflection and transmission analysis of the longitudinal elastic waves. Using a rectangular solid waveguide with clamped boundary conditions, Yao *et al.* [18] demonstrated that extreme low frequency bandgap of the clamped waveguide can be attributed to NMD that follows the Drude-form below a cutoff frequency. For EMM with complex microstructures, Liu *et al.* [19] developed a finite element (FE)-based effective medium model to obtain the effective dynamic material properties. More recently, Yang *et al.* [20] designed a new class of active EMM with shunted piezoelectric patches in which bandgaps can be actively controlled and tuned by varying effective stiffness constant of the linear spring through appropriately selecting the value of negative capacitance of the piezoelectric patch.

In two-dimensional (2D) and three-dimensional (3D) EMMs, the LR-based bandgaps may not occur in the same frequency range when the waves propagate along different directions, which implies that the resonant frequencies of the microstructure are different along principle directions and therefore, the effective mass density is anisotropic in the EMM. Based on the relations between the effective mass density and the LR microstructures, the anisotropic effective mass density of an EMM can be achieved by changing position or distribution array of the microstructure in a unit cell. A conceptual microstructural design of the EMM with anisotropic mass density is a 2D mass-in-mass lattice system consisting of two different elastic springs in the two principle directions. The first appearance of this microstructural design was made explicitly by Milton and Willis [14].

Then, Huang *et al.* [21] modeled the lattice system as an equivalent 2D elastic solid with its effective mass density characterized as a second-order tensor to describe the dynamic behavior of the original lattice system in all directions. A multi-displacement microstructure continuum model was proposed [22] and the anisotropic effective dynamic mass density tensor of a continuous EMM made of lead cylinders coated with elliptical rubbers in an epoxy matrix was calculated based on the microstructure continuum model [23]. In addition, Milton [24] has shown that all mechanical materials can in principle be synthesized by combing pentamodes that are artificial special solid with almost infinitely large ratio of the bulk modulus to the shear modulus. By building 3D pentamode metamaterials, mass density and bulk modulus can be tailed independently over a large range [25,26]. With 3D dilational EMM, an ultimate Poisson' ratio of -1 has been experimentally demonstrated [27].

Most designs of the EMM devices are based on the bulk waves that propagate in infinite or semi-infinite media with no boundary effects considered. However, in the real world, the wave medium is always finite, such as plate-like structures where the propagations of elastic waves are guided by two parallel free surfaces. On one hand, reflections on the two free surface boundaries will generate different Lamb wave modes and therefore complicate the problem. On the other hand, studies on plate-like structures consisting of bandgap materials are very important due to their more promising applications in the real-world engineering fields. Compared with an EMM plate, elastic wave propagation in the PC plate has been well studied by many researchers. The band structure of a 2D solid/solid PC plate has been analyzed by using the FE method [28]. Hsiao *et al.* [29] studied the band structure of steel/epoxy PC plates experimentally. Good agreement with the numerical simulation was found. Due to the wave attenuation mechanism in PC plates being attributed to the Bragg scattering bandgaps, the wave isolation ability of PC plate is limited in the mid-high frequency ranges. Different LR-based microstructural designs of EMM plates were proposed to block low frequency guided waves as well as control wave propagations in thin plates. Such designs can be cataloged into three groups: perforated microstructural design [30,31,32], stubbed microstructural design [33,34,35], and binary/ternary insert microstructural design [36,37].

In this paper, we present a comprehensive review of the microstructural designs of LR-based EMM plates and their potential applications in low frequency guided wave attenuation, subwavelength-scale wave manipulation, and energy trapping. The paper is arranged in five sections including this introduction: in [Section 2](#), the relation between the LR mechanism and the abnormal effective material properties of EMMs are explained through simple mass-spring lattices; in [Section 3](#), three groups of LR-based microstructural design for EMM plates are reviewed; in [Section 4](#), the potential applications of the EMM plates with the reviewed microstructures are discussed. Finally, conclusions are presented in [Section 5](#).

2. Effective material properties of locally resonant EMMs

In order to explain the origin of the abnormal effective material properties of LR EMMs, such as NMD and anisotropic mass density and their effects on the wave propagations, simple mass-spring models have been studied [21,38]. Negative effective mass can be demonstrated in a 1D mass-in-mass model while the anisotropic effective mass can be explained through the analysis on a 2D mass-spring lattice.

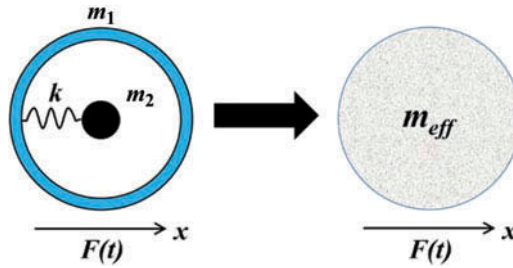


Figure 1. Single spring-mass system and its effective single mass model. Taken from Huang *et al.* [38].

2.1. One-dimensional mass-in-mass model and negative effective mass

Consider a single mass-in-mass unit as shown in Figure 1. Both masses m_1 and m_2 are rigid and the spring with linear spring constant k is massless. $F(t)$ is an external harmonic force with frequency ω and the mass-in-mass unit moves only along x direction. For the steady-state harmonic movement, the governing equation can be written as:

$$\left[\bar{F} + \left(m_1 + \frac{k}{\omega_0^2 - \omega^2} \right) \omega^2 \bar{u} \right] e^{-i\omega t} = 0, \quad (1)$$

where \bar{F} and \bar{u} are the amplitudes of the harmonic external force and the harmonic displacement along x -direction, respectively. $\omega_0 = \sqrt{k/m_2}$ is the LR frequency of the inner mass m_2 . When the mass-in-mass unit is represented by an equivalent model with single effective mass m_{eff} that is defined to produce the same displacement of m_1 in the lattice system, the corresponding governing equation for the equivalent model can be represented as:

$$\left[\bar{F} + m_{\text{eff}} \omega^2 \bar{u} \right] e^{-i\omega t} = 0 \quad (2)$$

Therefore, the effective mass can be obtained by comparing Equations (1) and (2):

$$m_{\text{eff}} = m_1 + \frac{m_2 \omega_0^2}{\omega_0^2 - \omega^2}. \quad (3)$$

It can be found that the effective mass becomes negative when the frequency ω approaches the LR frequency ω_0 . According to Newton's second law of motion, the acceleration would be in the opposite direction to the external force when the negative mass occurs therefore the propagating wave is prevented.

2.2. Two dimensional mass-spring lattice and anisotropic effective mass

In a 2D mass-spring lattice as shown in Figure 2, two different massless springs with spring constants k_1 and k_2 connect the inner mass m_2 to the outer rigid mass m_1 along the horizontal (x) and the vertical (y) directions, respectively. If an equivalent anisotropic lattice with different effective masses along x - and y -directions is defined, the effective masses along the two principal directions can be obtained as [21]:

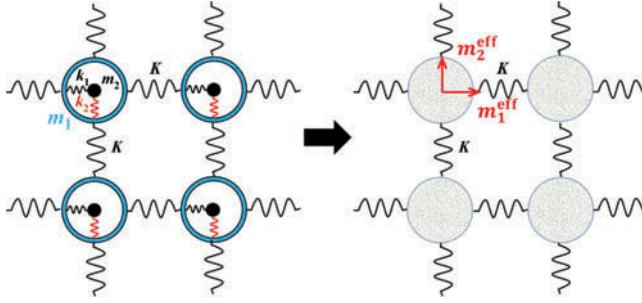


Figure 2. 2D mass-in-mass lattice system and effective medium with anisotropic effective mass.

$$m_1^{\text{eff}} = m_1 + \frac{m_2 k_1}{k_1 - m_2 \omega^2} \quad (4a)$$

$$m_2^{\text{eff}} = m_1 + \frac{m_2 k_2}{k_2 - m_2 \omega^2}, \quad (4b)$$

respectively. Comparing Equation (4a) and (4b), it is noticed that m_1^{eff} and m_2^{eff} are generally different. In a quasi-static case, the effective mass is almost isotropic. When the frequency approaches either LR frequency $\omega_{0,1} = \sqrt{k_1/m_2}$ or $\omega_{0,2} = \sqrt{k_2/m_2}$, the anisotropy of the effective mass becomes much stronger. In a certain frequency range, the effective masses along the two principal directions may have opposite signs. Therefore, the anisotropy between the effective mass densities along different principle directions of the lattice system is mainly caused by the difference between the LR frequencies that can be tuned through the design of the internal springs in the 2D lattice system.

3. Microstructural designs of locally resonant EMM plates

The mass-spring models perfectly complete their job that is illustrating the critical relation between negative effective material properties and the LR mechanism. However, applying these discrete designs into realistic engineering structure that requires high mechanical strength is unreliable and may introduce safety hazards. Therefore, designing an EMM with continuum medium having enough elastic strength is very critical for real-world engineering applications. In this section, various microstructural designs of solid EMMs in plate-like structures are reviewed and cataloged into three groups: perforated design, stubbed design, and binary/ternary insert design.

3.1. Perforated microstructural design

By periodically drilling holes through a metal plate, a PC bandgap can be created based on the Bragg scattering mechanism [39]. When the guided plate wave at the Bragg bandgap region hits the periodic holes, the reflected waves interfere with each other destructively and therefore, no propagating wave can be found in the PC plate. In order to generate the destructive interference of the reflected guided waves, the size of the through hole needs to be comparable with the wavelength of the guided wave that makes the PC plate impractically large and heavy at low frequency range. In order to produce a

low-frequency bandgap with a compact unit cell size, LR microstructures can be introduced into the perforated unit cell of the PC plate that can exhibit spectral gap at frequencies two orders of magnitude lower than those by Bragg scattering.

Zhu *et al.* [30] introduced a cantilever-mass LR microstructure inside the perforated cell and, therefore, both in-plane and out-of-plane guided waves are forbidden in the low frequency range. Inspired from the well-studied three-phase EMM unit cell consisting of rubber-coated lead core embedded in an epoxy matrix, they proposed a single-phase EMM unit cell consisting of only one medium – stainless steel and used cantilever-mass microstructure to introduce the LR motion. In order to study the working mechanism of the proposed single-phased EMM plate and to provide an optimized design for the low-frequency bandgap application, a FE-based dispersion calculation method was applied to five unit cells with different microstructure configurations, as shown in the second row in Figure 3.

In Figure 3 (a), the unit cell is a plate with an interior square cutout. Based on the unit cell in Figure 3 (a), an interior cantilever is subsequently added in the unit cell as shown in Figure 3 (b). In Figure 3 (c)–(e), the unit cell is a plate with an interior cantilever-mass system. As shown in Figure 3 (c)–(e), the masses at the tips of the cantilevers are m_1 , $m_2 = 2m_1$, and $m_3 = 3m_1$, respectively. The thin plate was made of stainless steel ($\rho = 8000 \text{ kg/m}^3$, $E = 193 \text{ GPa}$, and $\nu = 0.31$) with the thickness $h = 1 \text{ mm}$. Thirty unit cells in length direction and two unit cells in width direction were used for the simulations. The spacing of the adjacent unit cells is $a = 5.6 \text{ mm}$.

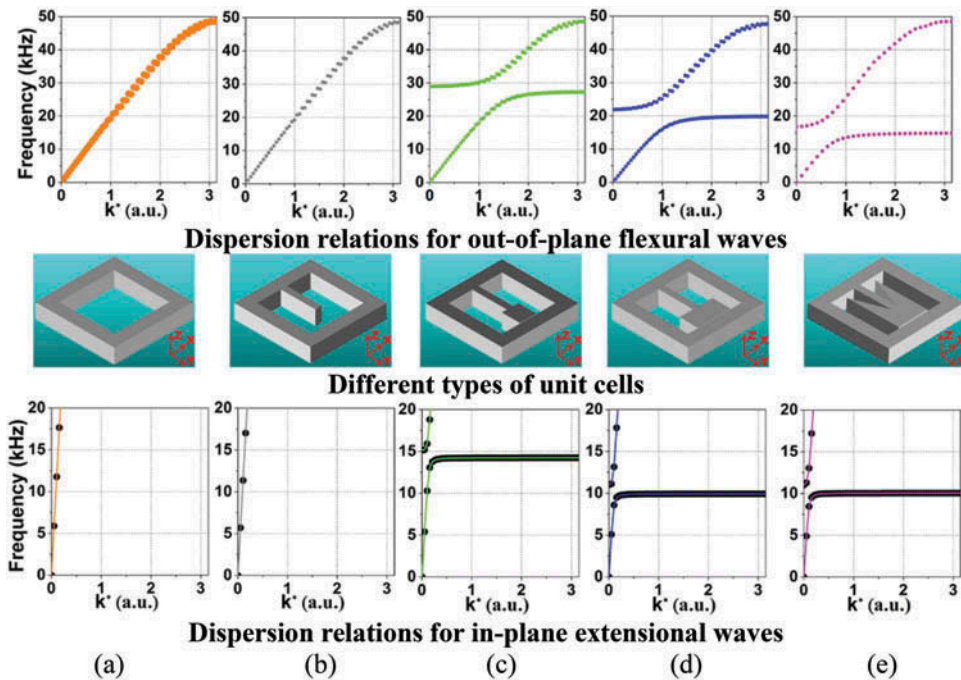


Figure 3. Dispersion relations of a thin plate with different types of unit cells: (a) only an interior square cutout, (b) added interior cantilever, (c) added interior cantilever with a tip mass m_1 , (d) added interior cantilever with a tip mass $m_2 = 2m_1$, (e) added interior cantilever with a tip mass $m_3 = 3m_1$. Taken from Zhu *et al.* [30].

Commercial FE software, ANSYS v11.0 was used for the simulation. In the FE simulation, the 3D solid element SOLID45 was chosen to discretize the unit cell of the EMM plate and five elements were used in the thickness direction. Manual mesh strategy was used to better control mesh density and element shape for the complex interior cantilever-mass geometry. Guided waves propagate along the x -direction as shown in Figure 3. The dispersion relations of the metamaterial plates with different types of unit cells for out-of-plane flexural waves and in-plane extensional waves are plotted in the first row and the third row in Figure 3, respectively. The phase velocities of the out-of-plane and in-plane guided waves in Figure 3 (a) are 670 m/s and 3900 m/s, respectively. Comparing with the phase velocities measured on the pure stainless steel plate, the interior square cutout reduces the effective elastic modulus of the unit cell hence decreases the phase velocities of the guided waves propagating along the plate. Attention is focused on the frequency range near the bandgap. The normalized wave number k^* is defined as $k^* = k \cdot a$, where k is the wave number. It can be noticed that no low-frequency bandgap can be found for the plates with the first two types of the unit cells. The low-frequency bandgap only appears in the plates that contain a mass at the tip of the cantilever in the unit cell. It is also noted that, as the tip mass increases, the bandgap frequencies are lowered. This can be easily explained by the resonance mechanism. For the cantilever-mass system, the LR frequency can be approximately estimated by $\omega_0 = \sqrt{\bar{K}_{\text{eff}}/M}$ where M is the tip mass, $\bar{K}_{\text{eff}} = 3EI/l^3$, E , I and l are elastic modulus, moment of inertia and length of the cantilever in Figure 3 (e), respectively. It should be mentioned that the moment of inertia I for in-plane wave is different from that of the flexural wave.

LR mechanisms cannot only form low frequency bandgaps but also introduce slow propagating modes inside the complete PC bandgaps with specially designed resonant microstructures. By replacing the periodical through holes in the PC plate with blind holes, Sun *et al.* [31] proposed an LR PC plate with a membrane type resonant microstructure in the unit cell to propagate resonant slow modes of concentrated acoustic energy. Figure 4 (a) demonstrates the schematic of the LR PC plate's unit cell. The unit cell contains a cylindrical hole and a membrane at one end of the hole. A steel specimen consisting of 16×10 unit cells were made by mechanical machining, as shown in Figure 4 (b). The lattice constant of the unit cell is $a = 9.52$ mm. The radius of the blind hole is $r = 4.475$ mm. The thickness of the plate and the membrane is $H = 5.05$ mm

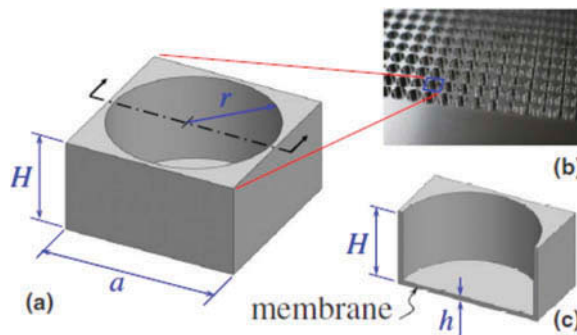


Figure 4. (a) Schematic of the unit cell of the square-lattice PC plate with periodic membranes. (b) Picture of the specimen. (c) Full section view of the unit cell. Taken from Sun *et al.* [31].

and $h = 0.29$ mm, respectively. The small thickness ratio between the plate and the membrane $h/H = 1/17.4$ makes the rigidity of the membrane very weak comparing with that of the rest of the plate.

The band structures of the PC plate with through holes and the LR PC plate with blind holes are shown in Figure 5 (a) as solid curves and dot curves, respectively. Commercial FE software, COMSOL MULTIPHYSICS (COMSOL Inc., Burlington, MA, USA) was used to obtain the band structures. In the calculation, the mass density, Young's modulus, and Poisson's ratio of steel were set to be 7750 kg/m^3 , 226 GPa , and 0.29 , respectively. Bloch periodic boundary conditions [40] were applied to the unit cell shown in Figure 4 (a). In Figure 5 (a), some near-flat bands can be found in the band structure of the LR PC plate, which are labeled by A , $B1$, $B2$, $C1$, $C2$, D , $E1$, $E2$, and F . These bands are associated with the vibration modes of the membranes that interact with the propagation modes of the PC plate and, therefore, result in additional bands in the band structure of the LR PC plate. When one compares the band structure of the PC plate and that of the proposed LR PC plate, eigenmodes of the LR PC plate, the modes F , can be found in the complete PC bandgap between 173 and 212 kHz. It should be noticed that these eigenmodes are not standing waves of energy localized inside the membranes but are propagating resonant modes with very slow group velocities. Figure 5 (b) and (c) shows the mode shapes of the resonant slow modes F labeled on the band structure in Figure 4 (a). The same periodic boundary conditions were used in the simulations of the mode shapes. The patterns of the mode shapes coincide with the eigenmodes of a clamped circular membrane that indicates that their eigen

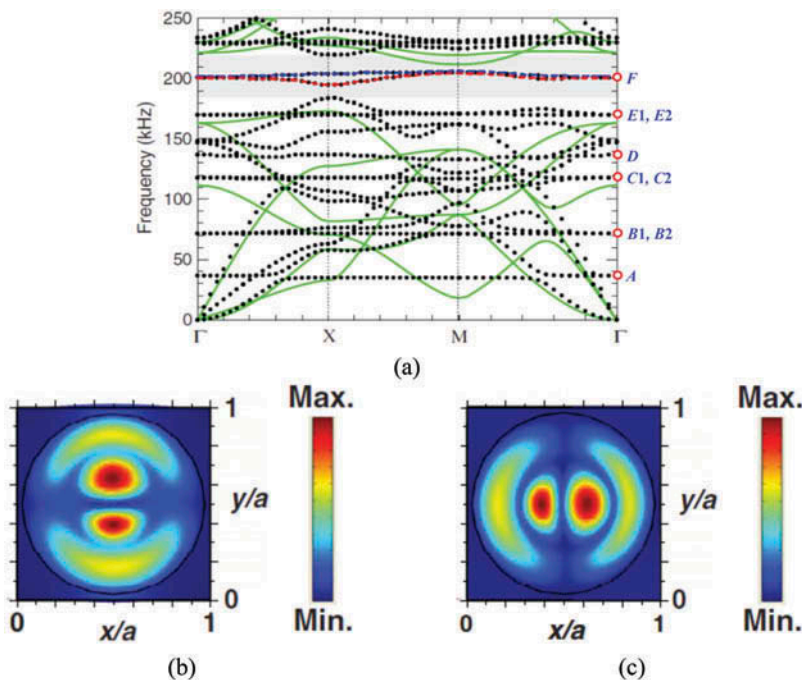


Figure 5. (a) Band structures of the PC plate with through holes (solid curves) and the LR PC plate with blind holes (dot curves). (b) Mode shapes of the lower resonant slow mode (red band). (c) Mode shapes of the higher resonant slow mode (blue band). Taken from Sun *et al.* [31].

frequencies of resonance are relevant [36]. According to the symmetries of the mode shapes, the resonant membrane modes can be classified into monopole, dipole, quadrupole mode, and so on. The red and blue bands of the modes F are found to be the lower and higher second-order dipole modes, respectively.

Most recently, Zhu *et al.* [32] introduced a subwavelength microstructure in a perforated hexagonal unit cell to produce simultaneous translational and rotational resonances and, therefore, create a double-negative EMM plate. The schematic top view of the unit cell of the proposed EMM plate is shown in Figure 6 (a). The unit cell is designed by properly slot-cutting in a hexagonal area and forming three chirally distributed ribs to connect the center piece (functioned as a mass) and the frame. The lattice constant is a , and widths of the slot, ribs, and frames are s , r , and t_f , respectively. In this design, the three ribs are very critical since they will induce not only the translational resonance but also the rotational resonance to the center piece, as shown in Figure 6 (b) and (c), respectively. Therefore, by carefully selecting the dimension of the chirally distributed ribs, it is possible to achieve and enhance simultaneous translational and rotational resonances at a desired low frequency range.

In order to calculate the effective medium parameters of the EMM plate with such a complicated microstructure, the use of analytical methods is not practicable. Instead, a numerical-based effective medium method based on the micromechanics approach is adopted, which is under the long-wavelength assumption [19]. The effective medium theory links the microscopic resonant structures to the EMM's macroscopic parameters. In the unit cell analysis, the global (macroscopic) stress, strain, resultant force, and acceleration of the unit cell can be numerically calculated by averaging local quantities on the external boundary of the hexagonal cell. Then, based on the constitutive relationship, the effective bulk modulus, shear modulus, and mass density of the proposed chiral EMM can be determined from the calculated macro-quantities. Based on the numerical-based effective model, the effective bulk modulus and mass density of the chiral EMM were calculated and are shown in

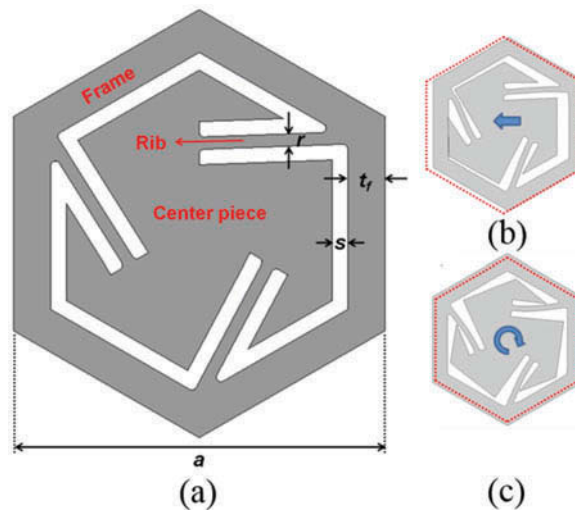


Figure 6. (a) Schematic top view of the EMM's unit cell. (b) The mode shape of the translational resonance. (c) The mode shape of the rotational resonance. Taken from Zhu *et al.* [32].

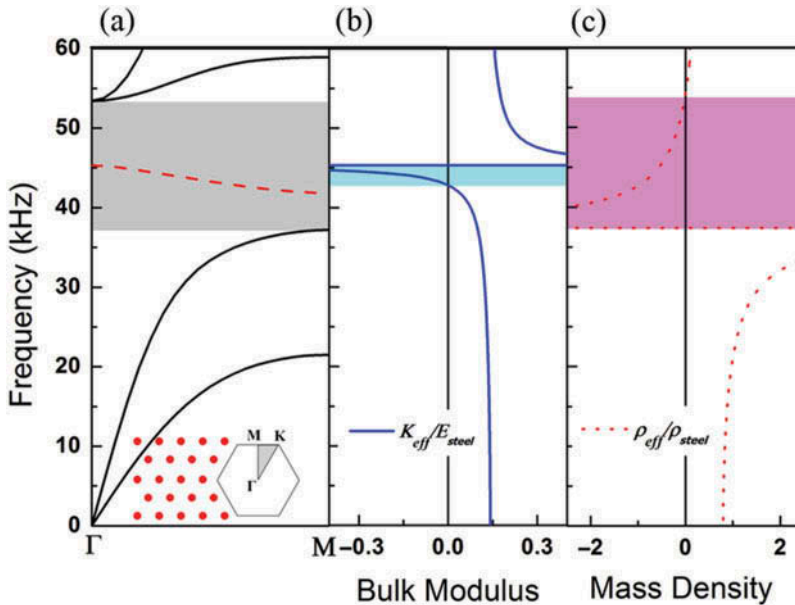


Figure 7. (a) Dispersion curves of the EMM plate along ΓM direction. (b) Effective bulk modulus of the chiral EMM. (c) Effective mass density of the chiral EMM. Taken from Zhu *et al.* [32].

Figure 7 (b) and (c), respectively. The effective mass density ρ_{eff} and bulk modulus K_{eff} were normalized with the density and Young's modulus of the single-phase medium (stainless steel), respectively. The dispersion curves of the system along the ΓM direction were also numerically obtained based on the Floquet theory, as shown in Figure 7 (a). The lattice array of the chiral EMM and its irreducible Brillouin zone (IBZ) were also inserted in Figure 7 (a).

As evidenced in Figure 7, the frequency range of the bandgap predicted from the dispersion calculation (gray area in 37.2–53.6 kHz) is almost the same as the frequency range with negative ρ_{eff} (pink area in 37.4–54.1 kHz) as shown in Figure 7 (c), which can be explained by the out-of-phase translational motion of the center piece against the frame. As shown in Figure 7 (b), K_{eff} becomes negative in the frequency range of 42.9–45.0 kHz (highlighted with blue color). The effective shear modulus μ_{eff} was calculated as 16.23 GPa in the considered frequency range with a small variation. Eventually, both effective longitudinal modulus $E_{\text{eff}} = K_{\text{eff}} + \mu_{\text{eff}}$ and effective mass density ρ_{eff} become negative in the regime from 43.6 to 45.0 kHz, which implies a negative band for the longitudinal wave in this frequency region. It is also noticed that the double-negative frequency region (43.6–45.0 kHz) is not the same as the total negative passband frequency region (the red dashed line, 41.8–45.0 kHz) from the dispersion curves, as shown in Figure 7 (a). The difference can be attributed to the strong chirality and anisotropy of the current microstructural design, which cannot be exactly captured by using the effective isotropic medium [41]. For the chiral topology, the number of the chirally distributed ribs, N_r , is an important parameter for the global property of the chiral EMM. The EMM becomes more isotropic when N_r is a larger value, while displaying stronger anisotropy when N_r is a smaller value.

3.2. Stubbed microstructural design

Although the perforated designs have the advantages of using single type of material and are easy to be fabricated, removing part of the pristine structure through perforation can significantly reduce the mechanical strength of the structure and, therefore, is strictly prohibited in many engineering applications such as structural health monitoring (SHM). In order to fabricate a practical plate-type EMM without sacrificing the strength of the original plate, local resonance is introduced into the PC plate with surface-bonded or stubbed microstructures.

Wu *et al.* [33] numerically and experimentally demonstrated the existence of complete bandgaps and resonances in a PC plate with a periodically stubbed surface. In their design, stubbed Al cylinders were periodically arranged in a square lattice on one side of a thin Al plate. Band structures of the unit cells with stubs of different heights were calculated along the ΓX direction to understand the influence of the stubs' height on the dispersion, as shown in Figure 8. Upon comparison with the dispersion relation of a homogeneous thin plate, as shown in Figure 8 (a), formation of the special coupling modes can be identified. For example, in Figure 8 (b), when the stub height $h_2 = 0.25 h_1$, the purple line marked with S0+A0 indicates the mode is transformed from the S0 mode and A0 modes shown in Figure 8 (a). Similarly, the yellow line marked with A0+S0+A1 in Figure 8 (b) denotes the mode is transformed from the A0, S0, and A1 modes. The evolution of the coupling modes as well as formation of level repulsions [42] can be identified by comparing Figure 8 (a–c).

In the numerical study, the height of the stubs was increased from one quarter of the plate thickness gradually up to ten times of the thickness. As the height of stubs increased, some resonances were formed, which resulted in slower wave velocity and flatter modes

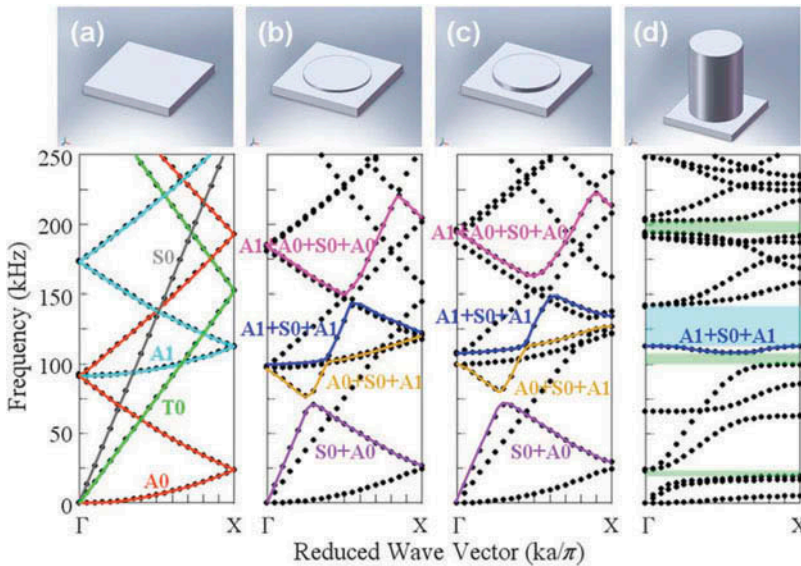


Figure 8. Dispersion relations of the thin PC plate with stubs of different heights along ΓX direction: (a) flat thin plate, (b) stub height $h_2 = 0.25 h_1$, (c) stub height $h_2 = 0.5 h_1$, and (d) stub height $h_2 = 10 h_1$. Lattice constant $a = 10$ mm, plate thickness $h_1 = 1$ mm, and diameter of the cylindrical stub is 7 mm. Taken from Wu *et al.* [33].

[43] near the edge of the Brillouin zone. It can be found that as the stub height approaches about triple the plate thickness, a narrow complete bandgap ranging from 167.5 to 171 kHz forms. Moreover, when the stub height is equal to nine times of the plate thickness, the complete bandgap is the largest, with a range from 119 to 157.5 kHz and a relative bandgap width equal to 0.278. When the stub height is ten times the thickness, a secondary large complete bandgap appeared, ranging from 119 to 143 kHz (blue region), and three partial bandgaps (green region) also appeared, as shown in Figures 8 (d) and 9.

By periodically depositing two-layer composite stubs on the surface of a thin plate, Oudich *et al.* [34] opened a complete bandgap at extremely low frequency range by the LR mechanism. The schematic view of the LR PC plate with two-layer stubs is shown in Figure 10. The proposed LR PC is constructed by depositing the cylinder resonant stubs squarely onto the surface of a thin epoxy plate. The stub is a composite cylinder with a uniform radius of r and a height of $h = h_1 + h_2$, where h_1 and h_2 are the thicknesses of the silicone rubber and Pb layers, respectively. The lattice constant of the unit cell is a , and the plate has a thickness of $e = 0.05a$. Because the stiffness of the capped Pb is far greater than that of rubber, the effective stiffness of the composite stub is determined mainly by

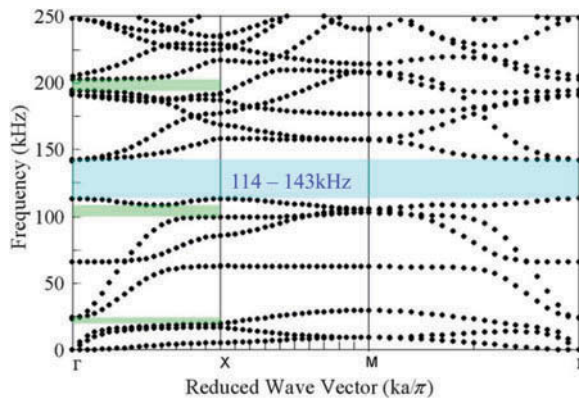


Figure 9. Dispersion relations of the thin plate with a periodic stubbed surface in a square array made of Al 6061 with $a = 10$ mm, $h_1 = 1$ mm, $h_2 = 10 h_1$, and $d = 7$ mm. Complete bandgap and partial bandgap along the ΓX direction are shown as the blue region and green region, respectively. Taken from Wu *et al.* [33].

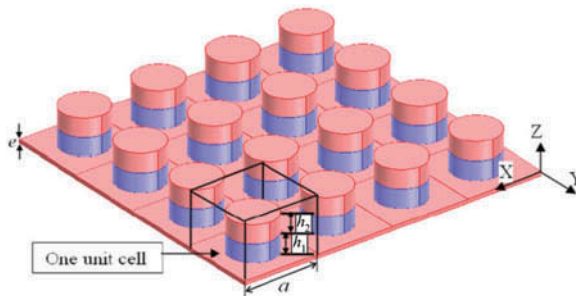


Figure 10. Schematic view of the LR PC plate with two-layer composite stubs. Taken from Oudich *et al.* [34].

the rubber layer. Comparing with the low frequency bandgap obtained in the single-layer stub LR PC plate like the one in Figure 8 (d), the bandgap in the two-layer composite stub LR PC plate can be pressed into even lower frequency region by either increasing the thickness of the Pb layer which is equivalent to increasing the mass of the stub or by increasing the thickness of the rubber layer which is equivalent to decreasing the effective elastic constant of the stub.

In Figure 11, the band structures for the composite stubs are given for fixed r and h_1 ($r = 0.3a$ and $h_1 = 0.1a$), but various values of h_2 ($h_2 = 0.1a, 0.2a, 0.3a$ and $0.4a$). It can be clearly found that the bandgap being pushed into lower frequency range as h_2 increases.

By changing the shape and the geometrical parameters of the stub, the location of the low frequency bandgap can also be shifted into the desired frequency range. Hsu *et al.* [35] numerically investigated a 2D LR PC plate composed of periodically arranged stepped resonant stubs. Because of the simultaneous mechanisms of the local resonances and Bragg scattering, the proposed LR PC plates exhibit low frequency forbidden bands and Bragg bandgaps.

Figure 12 illustrates the schematics of a unit cell of the LR PC plate. The unit cell is composed of stepped resonant stubs on a unit slab of thickness h . The resonant stub consists of two cylinder segments with different lengths and radii, termed as the neck and the cavity, respectively. l and r are the length and radius of the neck, respectively. L and R are those of the cavity, respectively. The lattice spacing between two nearby square lattices is a . Figure 13 shows the band structure of the unit cell described in Figure 12. The wave vectors are restricted within the x - y plane and point to the boundary Γ XM Γ of the IBZ [44]. Both the stubs and the thin plate are made of steel. Two complete bandgaps

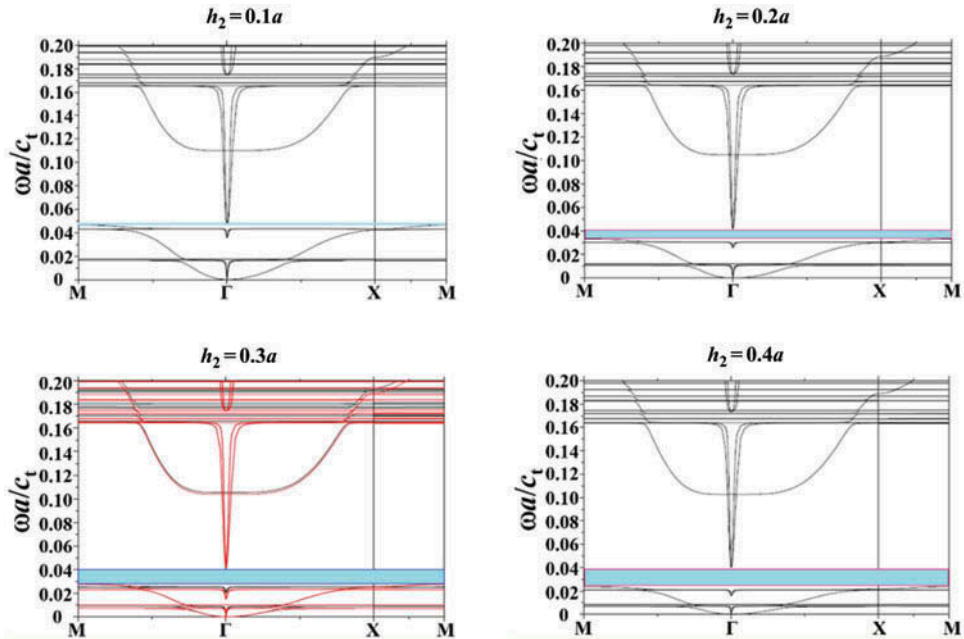


Figure 11. Band structures for LR PC plate with two-layer composite stubs. Taken from Oudich *et al.* [34].

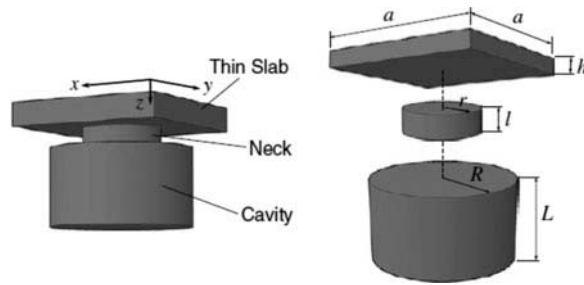


Figure 12. Schematics of the unit cell of the LR PC plate with stepped resonant stubs. Taken from Hsu *et al.* [35].

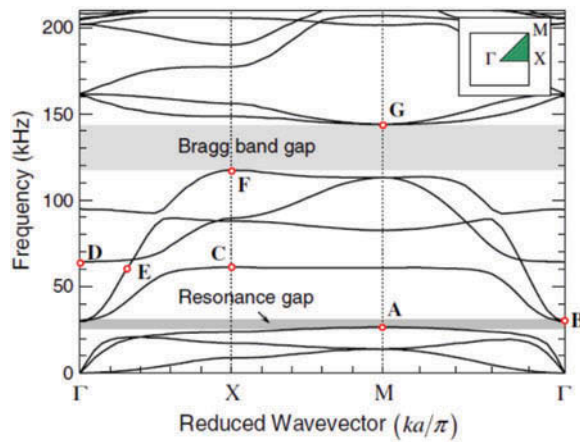


Figure 13. Band structure with two kinds of complete band gaps (LR and Bragg) of the PC plate with stepped resonant stubs. Taken from Hsu *et al.* [35].

can be found in the range from 26.4 to 30.2 kHz and range from 117.5 to 143.9 kHz. The lower gap is the local resonance gap while the higher gap is the Bragg gap. The effect of the geometrical factors on the variation of the bandgap width and frequency was also studied and both the widths and frequencies of the lower and higher bandgaps were found to be dependent on these geometrical factors [35].

3.3. Binary/ternary insert microstructural design

In 2000, Liu *et al.* [13] first demonstrated the extremely low frequency bandgap using an EMM with a ternary LR microstructure – soft-rubber-coated lead core embedded in epoxy matrix. The low frequency bandgap can also be made by a PC with binary LR microstructure. Wang *et al.* [16] investigated a binary 1D PC with periodic microstructure consisting of Pb and epoxy layers. A bandgap is observed at an extremely low frequency range due to the LR mechanism introduced by the large mismatch between the elastic modulus of the two media. Inspired by the 1D microstructural design, Hsu *et al.* [36] investigated the propagation of Lamb waves in 2D LR PC plates composed of periodic

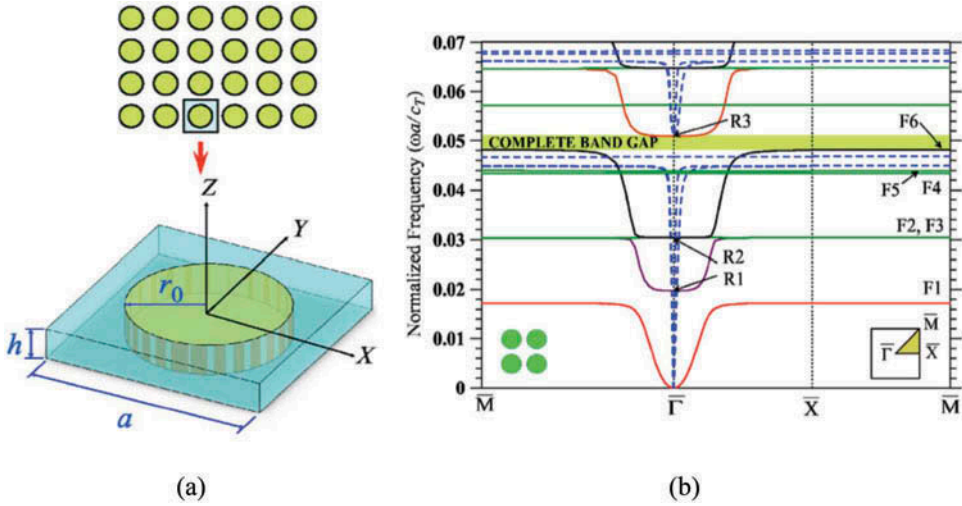


Figure 14. (a) Schematic of a unit cell of binary LR PC plate. (b) Band structure of Lamb waves in the LR PC plate with $r_0/a = 0.4$ and $h/a = 0.115$. Taken from Hsu *et al.* [36].

soft rubber fillers in epoxy host based on the plane wave expansion formulation utilizing Mindlin's theory [45].

The schematic of a unit cell of the proposed binary LR PC plate is illustrated in Figure 14 (a). The lattice constant and the radius of the circular fillers are denoted by a and r_0 , respectively. The plate thickness is h . In calculations of the band structures, the density ρ of soft rubber is assumed as 1300 kg/m^3 , and that of epoxy is 1180 kg/m^3 . The phase velocities of longitudinal and transverse waves in soft rubber are $c_L^r = 33 \text{ m/s}$ and $c_T^r = 5 \text{ m/s}$, respectively [46]. In epoxy, $c_L^e = 2534 \text{ m/s}$ and $c_T^e = 1157 \text{ m/s}$, respectively. Large mismatch between the wave velocities in the two material components leads to local resonance phenomenon inside the metamaterial unit cell [47]. With a properly selected ratio between the plate thickness and the lattice constant, such as $h/a = 0.115$, a complete bandgap can be obtained in the low frequency range from 0.04812 to 0.05095 which is two orders of magnitude lower than the that resulting from Bragg scattering, as shown in Figure 14 (b). The frequencies in the figure are given in the normalized unit $\omega a/c_T$, where $c_T = 1157 \text{ m/s}$. There are many flat bands in the band structure and they indicate the resonant frequencies of the localized plate mode. The flexure-dominated branches that have a larger out-of-plane component of displacement are labeled by F1–F6 and they exhibit sensitivity to the variation of the plate thickness. R1–R3 denote the flexure-dominated modes with a zero group velocity near the $\bar{\Gamma}$ point, which presents a localized pattern.

Based on the modifications of the well-known ternary EMM proposed by Liu *et al.* [13], Zhu *et al.* [37] designed EMM plates with anisotropic dynamic mass density. Figure 15 shows the unit cell of the ternary EMM plate with an elliptical coating layer. The in-plane x_1 and x_2 axes are parallel to the elliptical semimajor axis and the semiminor axis, respectively. This design introduces local stiffness anisotropy in the proposed unit cell that creates different LR frequencies $\omega_{0,1}$ and $\omega_{0,2}$ along the two in-plane principal directions of the EMM plate and, therefore, generates the anisotropic effective mass

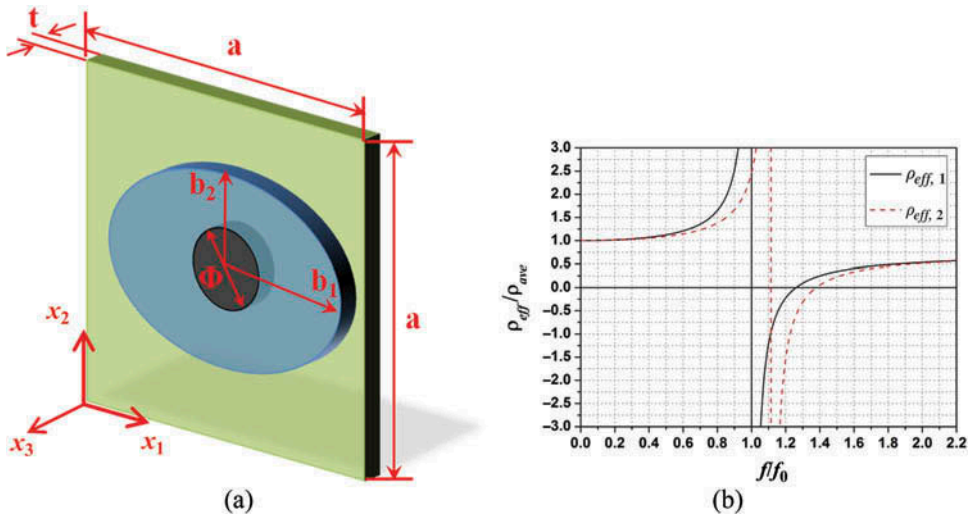


Figure 15. (a) Unit cell of the EMM plate with elliptical coating layer. (b) Normalized effective mass densities as functions of the normalized frequency along different principal directions. Taken from Zhu *et al.* [37].

density. By using a numerically based effective medium model [48], the normalized effective mass densities along x_1 and x_2 directions as functions of the normalized frequency are calculated, as shown in Figure 15 (b). In the figure, ρ_{ave} is the average static mass density for the composite and f_0 is the LR frequency of the microstructure along x_1 direction. It is noticed that $\rho_{eff,1}$ and $\rho_{eff,2}$ have different values in the normalized frequency range from $ff_0 = 0.4$ to $ff_0 = 1.8$. However, the anisotropic design is quite limited to the ratio of the semi-major axis to the semi-minor axis of the coating ellipse. To achieve a more strongly anisotropic effective mass density, a more modified microstructure design is needed.

Figure 16 (a) shows a new microstructure design in the elliptical coating layer with four symmetric micro-pores for greater anisotropy in mass density. The same geometrical and material parameters in Table 1 are used. The diameter of the micro-pore is $D = 2.15$ mm and the centers of the four symmetric micro-pores are located at $r = 3.13$ mm with the orientation angles being 25° , 155° , 205° , and 335° , respectively. Figure 16 (b) shows the in-plane normalized effective mass density of the EMM plate with the micro-pores as a function of the normalized frequency. Comparing with the results in Figure 15 (b), it can be observed that the lower band of the frequency range of $\rho_{eff,1}$ and $\rho_{eff,2}$ being different values keeps the same; however, the upper band of the frequency range is dramatically increased from $ff_0 = 1.8$ to $ff_0 = 3.0$, which shows that stronger anisotropy of the effective mass density can be achieved through the current microstructure design. The same lower band of the frequency range is expected because of the frequency normalization with respect to the average static mass density. It is also interesting to note that the effective mass density becomes isotropic when the frequency is close to the static case or much larger than the resonant frequencies. It should be mentioned that the anisotropy can be further tuned through the change of the positions, shapes, and sizes of the micro-pores in the coating layer and the inner mass.

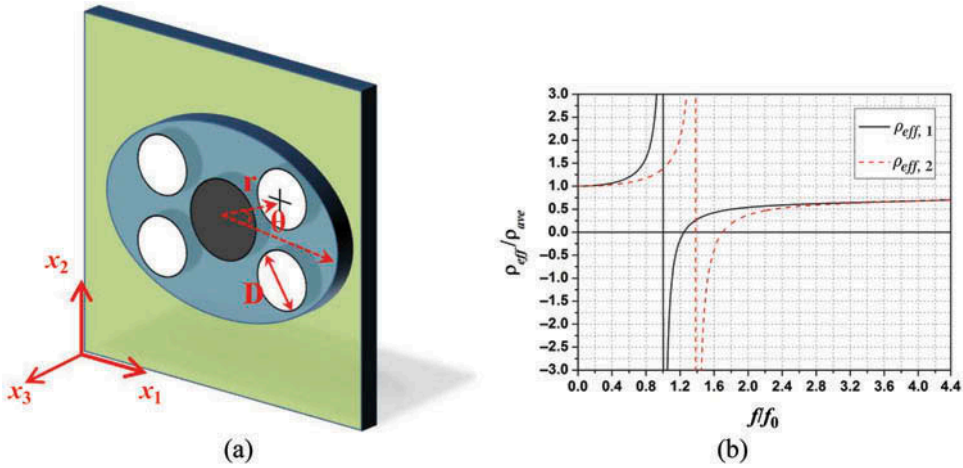


Figure 16. (a) Unit cell of the EMM plate with micro-pores in the coating layer. (b) Normalized effective mass densities as functions of the normalized frequency along different principal directions. Taken from Zhu *et al.* [37].

Table 1. Microstructure geometrical and material parameters.

Geometrical parameters			Material parameters		
a	11 mm		Matrix: aluminum	Coating: epoxy	Core: lead
b_1	4.95 mm	Mass density	2700 kg/m ³	11310 kg/m ³	11310kg/m ³
b_2	3.5 mm	Young's modulus	71GPa	0.595GPa	13GPa
Φ	3.175 mm	Poisson's ratio	0.32	0.38	0.435
t	3.175 mm				

4. Applications of locally resonant EMM plates

Designing EMM devices to control guided elastic wave propagation in finite medium with boundaries is very important for real-world engineering applications. In this section, we will review various engineering applications of LR EMM plates, such as low frequency guided wave attenuation, waveguide of Lamb waves, flat-lens focusing, subwavelength-scale negative refraction, and energy trapping.

4.1. Low frequency guide wave attenuation

By using the perforated LR microstructures in a single-phase thin steel plate as shown in Figure 3 (e), Zhu *et al.* [30] demonstrated the low frequency wave attenuation ability of the EMM plate for both in-plane and out-of-plane guided waves. Numerical investigation was conducted by considering free harmonic in-plane wave propagation. Since the wavelength of the harmonic wave generated at the excitation frequency is much larger than the size of the microstructure of the plate, the EMM plate can be regarded as an effectively homogeneous continuous medium. For a harmonic longitudinal wave propagating in the x -direction, let the global in-plane displacement at the $(j)^{\text{th}}$ unit cell of the EMM plate be expressed as:

$$u_x^{(j)} = Be^{-i\omega t}, \tag{5}$$

where ω is angular frequency and B denotes wave amplitude. Then, the wave motion of the $(j + n)^{\text{th}}$ unit cell can be written as:

$$u_x^{(j+n)} = Be^{i(nka-\omega t)}, \tag{6}$$

where n is an integer representing the periodic number of unit cells, k is the wave number, and a is the lattice constant of the unit cell. If the excitation frequency is in the bandgap, then the wave number would become complex, that is, $ka = \alpha + i\beta$, and we have

$$\left| \frac{u_x^{(j+n)}}{u_x^{(j)}} \right| = e^{-n\beta}, \tag{7}$$

From Equation (7), it can be noticed that the displacement decays spatially as an exponential function when wave frequency is within the bandgap. In order to confirm the attenuation mechanism, a numerical analysis was performed by extracting displacements of the nodes along the wave propagation direction. In the numerical simulation, the metamaterial plate consisted of 30×2 unit cells with cantilever-mass microstructures. The plate was free at one end and the sinusoidal displacement excitation was applied at the other end of the plate. The spatial attenuation of the EMM plate under different exciting frequencies for the x -directional in-plane extensional wave is shown in Figure 17 (a). In the figure, the normalized displacement field is defined as $U^* = |u_x|/|u_{x0}|$ with u_x being displacement responses at different locations in the plate and u_{x0} the excitation displacement. To gain a direct insight of the spatial attenuation, the entire deformation fields in the EMM plate for different excitation frequencies are schematically displayed in

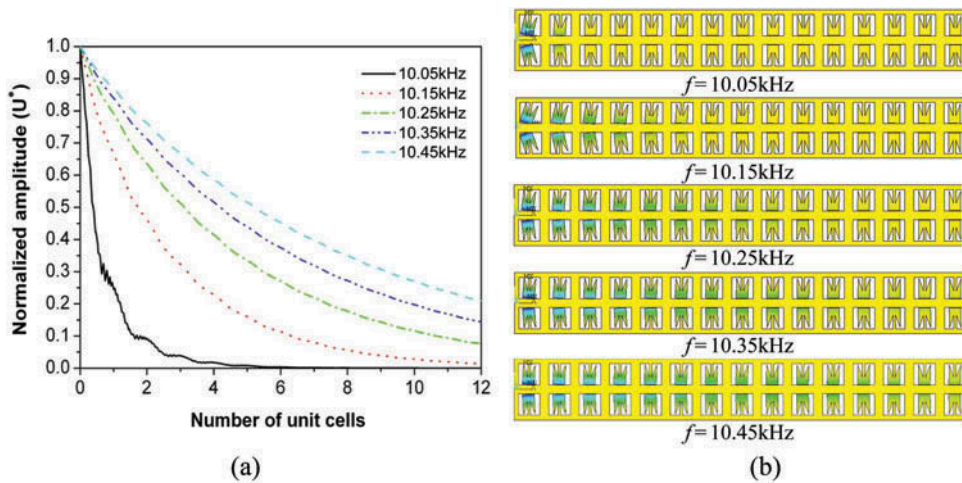


Figure 17. (a) Normalized x -directional in-plane guided wave displacements at different frequencies; (b) x -directional displacement fields in the plate at different frequencies. Taken from Zhu *et al.* [30].

Figure 17 (b). It is obvious that the displacement response exhibits significant attenuation when the frequency is close to the LR frequency (10.05 kHz for the in-plane extensional wave from numerical simulation in Figure 3 (e)). The wave amplitude is seen to decay significantly within two or three unit cells when the excitation frequency is almost equal to the resonance frequency. Similar phenomenon can be also observed for the out-of-plane guided wave propagation. From the figure, it can be observed that most of the energy is localized in the cantilever inclusion near where the load is applied. Very little energy is stored in the host plate. Since the system is purely elastic with the absence of material damping, the attenuation process within the bandgap provides an effective damping. This phenomenon has been explained by Huang *et al.* [38] using a discrete mass-spring metamaterial model.

4.2. Waveguide of Lamb waves

By using a LR stubbed microstructural design similar to those discussed in Section 3.2, Oudich *et al.* [49] constructed an LR PC plate to present an analysis of the Lamb waves in both straight and bending waveguides. First, a straight waveguide was created by removing three rows of the LR stubs in the Lamb wave propagation direction (ΓX direction). Due to the removal of the three rows of stubs, a confined mode was introduced in the complete bandgap of the original PC. In order to clearly understand what is happening in the waveguide, the total displacement fields of the LR PC in different reduced wave numbers, inside and outside of the complete bandgap, were demonstrated in Figure 18 (a) and (b), respectively. Inside the bandgap, the displacement field shows a very confined mode in the waveguide even though there is a very small penetration of waves in the first neighboring stubs of the waveguide, as shown in Figure 18 (a). When the frequency moves away from the bandgap, the confined mode in the waveguide becomes less confined and propagates throughout the LR PC plate, as shown in Figure 18 (b). It is noticed that waveguiding in a LR PC plate can be achieved for a larger waveguide width than for the traditional PC waveguide based on Bragg scattering. This result can be supported by the fact that in the LR mechanism, one encounters larger wavelengths compared to the PC lattice period.

The bent waveguide through four 90° corners was also investigated. Figure 19 (a) and (b) shows the schematic of the bent waveguide and the displacement field for the guiding mode, respectively. The width of the waveguide is still three rows. From the figure, perfect guiding of Lamb waves can be achieved by using the LR PC bent waveguide.

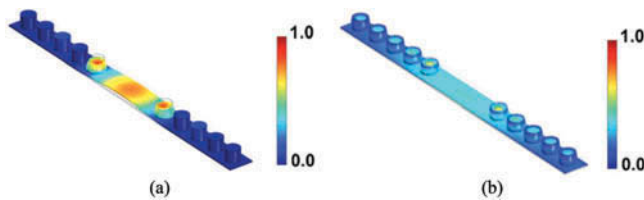


Figure 18. Absolute value of the total displacement field of the defect mode (a) inside and (b) outside the bandgap. Taken from Oudich *et al.* [49].

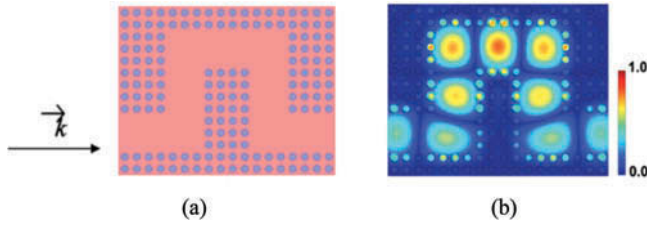


Figure 19. Schematic of the bent waveguide made in LR PC plate. (b) Absolute value of the displacement field for the guiding mode. Taken from Oudich *et al.* [49].

4.3. Flat-lens focusing

Flat-lens focusing of Lamb waves has great potential applications in the field of SHM by increasing the SNR for detecting plate damage in high resolution. Focusing of the lowest flexural (or antisymmetric) Lamb waves in the gradient-index (GRIN) PC plate has been successfully demonstrated [50,51,52]. However, the inherent Bragg scattering mechanism of PC significantly increases the size of the lens at low frequency range and, therefore, makes it unsuitable for embedded monitoring system. In addition, many proposed GRIN PC lenses are based on the perforated designs that degrade the strength of the pristine structure. In order to overcome the problems, Yan *et al.* [53] proposed a LR EMM flat lens by bonding a 2D planar array of the two-layer composite stubs (Pb disc deposited on the silicon rubber layer) for the A0 Lamb wave focusing. Different from the hyperbolic refractive index used in PC flat lenses, the proposed EMM lens for Lamb waves focusing is to vary effective mass densities that can be tailored from different EMM cells. The effective out-of-plane mass density profile is in the form of a hyperbolic secant as:

$$\rho_{\text{eff}} = \rho_{\text{eff},0} \text{sech}^2(\alpha y), \tag{8}$$

where $\rho_{\text{eff},0}$ is the effective mass density of the reference cells in an array located at $y = 0$ and α is the gradient coefficient characterizing the degree of focusing. Figure 20 (a) shows the hyperbolic secant effective mass density profile. Figure 20 (b) shows the schematic view of the proposed EMM flat lens.

A FE method was adopted to simulate the 30 kHz A0 wave mode through the EMM plate. Displacement contours in out-of-plane z -direction at different time steps were used to demonstrate the flat-lens focusing phenomenon, as shown in Figure 21. It can be

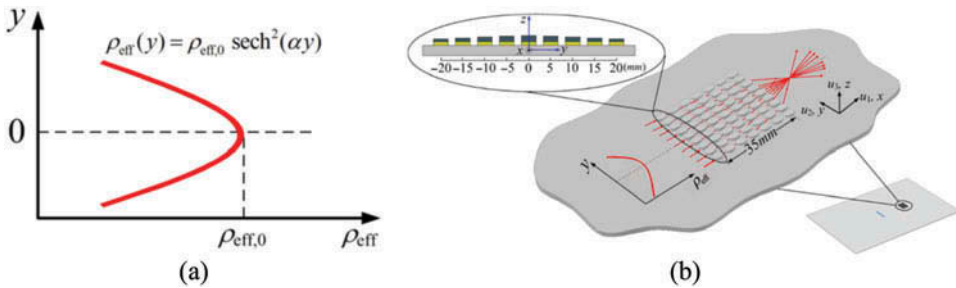


Figure 20. (a) Hyperbolic secant effective mass density profile. (b) Schematic view of the proposed EMM flat lens. Taken from Yan *et al.* [53].

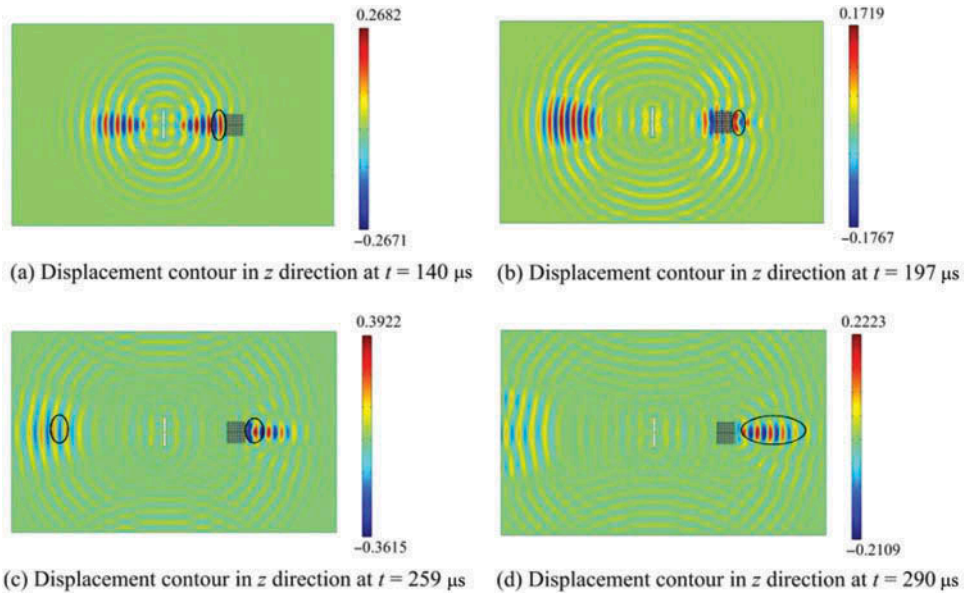


Figure 21. Snapshot of out-of-plane displacement contour (μm) for Lamb waves focusing. Taken from Yan *et al.* [53].

observed in Figure 21 (b) that Lamb waves are bent gradually toward the center axis. Figure 21 (c) shows that the waves are eventually focused to a focal spot (area) with the largest out-of-plane displacement of $0.3922 \mu\text{m}$ that is more than two times than the amplitude of the backward propagating waves without focusing.

4.4. Subwavelength negative refraction

The discovery of negative refractions of EM waves and mechanical waves opens exciting avenues to various applications such as super-resolution imaging to overcome diffraction limit [54,55,56,57]. Although a large amount of research work has been reported on negative refraction of EM waves and acoustic waves in fluid-like media, relatively fewer experimental demonstrations exist on negative refraction of elastic waves in solid media where the coupled longitudinal and transverse waves bring challenging but richer wave phenomena. Zhu *et al.* [32] experimentally achieved negative refraction of the longitudinal elastic waves at the deep-subwavelength-scale in the LR EMM fabricated in a stainless steel plate. The microstructural design of the proposed EMM is one of the perforated designs discussed in Section 3.1 and is shown in Figure 6 (a). With the double-negative effective material properties produced by the simultaneous translational and rotational resonances at a desired low frequency range, the negative refraction was obtained at a deep subwavelength scale, as shown in Figure 22 (a). The longitudinal elastic wave was incident from the left side of the EMM prism and a 50-cycle narrow band tone burst excitation signal with the central frequency inside the double-negative region (red dashed band in Figure 7 (a)) was used. Figure 22 (b) shows the positive refraction when the central frequency of the excitation signal was outside the double-negative region.

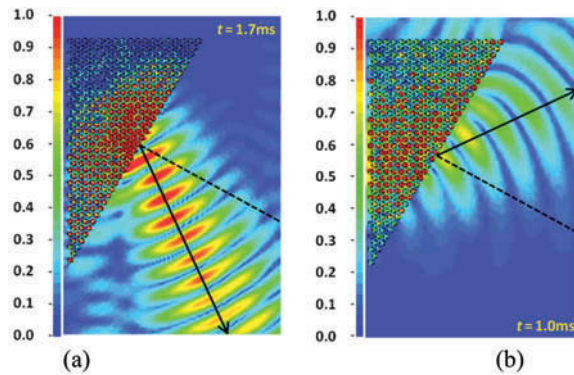


Figure 22. (a) Negative refraction of the longitudinal elastic wave at an excitation frequency inside the double-negative region. (b) Positive refraction of the longitudinal elastic wave at an excitation frequency outside the double-negative region. Taken from Zhu *et al.* [32].

Experimental validations were conducted on a prism-shaped EMM plate fabricated in a thin stainless steel (Grade 304) plate. The specimen was manufactured by using a precision laser cutting system, as shown in Figure 23 (a). Zoomed-in views of the specimen at different scale bars are demonstrated in Figure 23 (b–c). A 3D laser scanning vibrometer (Polytec PSV-400-3D) was used for the experimental measurement of the velocity field on the fabricated EMM plate. The experimentally measured velocity fields show the same negative refraction phenomena and therefore validated numerical simulation and the microstructural design.

4.5. Subwavelength energy trapping

By removing one scatterer, a defect is created inside the PC and the energy within the frequency bandgap is confined inside the defect region in the bandgap. This energy trapping phenomena through the defect mode has been recently studied in a

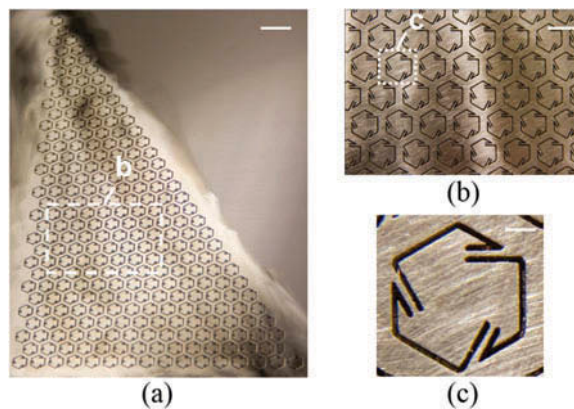


Figure 23. (a) The fabricated triangular array of the EMM. Scale bar, 20 mm. (b) Zoomed unit cells. Scale bar, 10 mm. (c) Zoomed single unit cell. Scale bar, 2 mm. Taken from Zhu *et al.* [32].

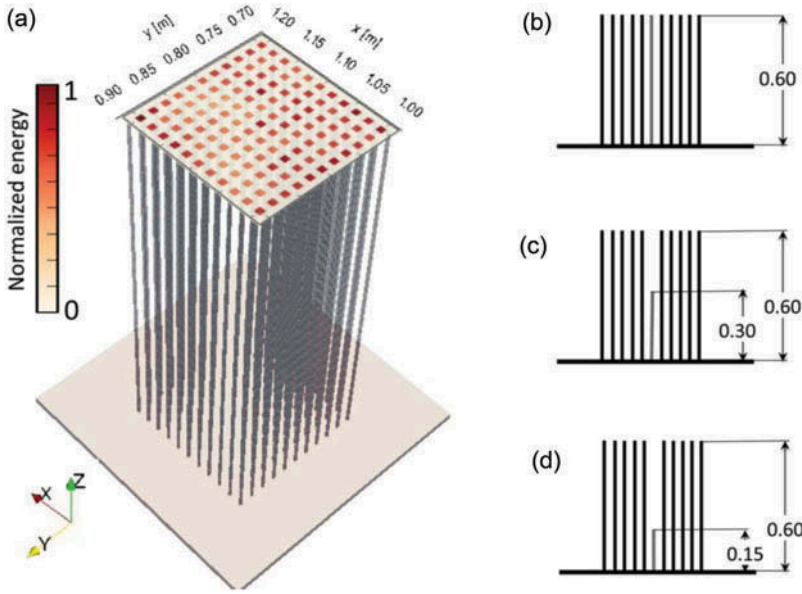


Figure 24. (a) EMM plate with 11×11 subwavelength resonator attached to the surface of the Al plate. The value of the energy beam is superimposed on the EMM region. (b) Slice view of the reference EMM (no defect). (c) Slice view of the defect EMM with short central beam. (d) Slice view of the defect EMM with shorter central beam. Taken from Colombi *et al.* [58].

subwavelength EMM plate by Colombi *et al.* [58]. The EMM was realized by a stubbed microstructural design by attaching a 11×11 vertical narrow beams ($L = 60$ cm long, 4×4 mm square section) perpendicular to a 6-mm-thick Al plate, as shown in Figure 24 (a). In order to demonstrate the energy trapping inside the EMM region, the local energy E in each resonant beam was calculated as:

$$E(x, y) = \sum_{i=1}^3 \sum_{z_i=0}^L \int_{t_0}^T u_i^2(x, y, z_i, t) dt, \quad (9)$$

where L is the total length of the beam, (x, y) which are selected pairs on the x - y plane, z_i is the vertical component that is regularly sampled between 0 and L , u_i is the i th component of the displacement and $[t_0, T]$ is the time window of the integration on the transient response. Two configurations of the defect were analyzed by applying different lengths for the beam in the defect unit cell, as shown in Figure 24 (c-d).

The anticipated energy trapping can be found in the plot of $E(x, y)$ in Figure 25. Figure 25 (a) shows the energy is concentrated in the short central beam resonator that has the height shown in Figure 24 (c). Figure 25 (b) shows the energy concentration in the configuration shown in Figure 24 (d). In order to distinguish the energy trapping in EMM plate from that in PC plate that relies on the periodicity due to the Bragg scattering, the configuration of Figure 24 (c) was modified with a spatially random arrangement and the result energy plot is shown in Figure 25 (c). It can be found that the energy boost is similar to the ordered case, and hence this confirms that the local resonances are at the origin of the phenomenon.

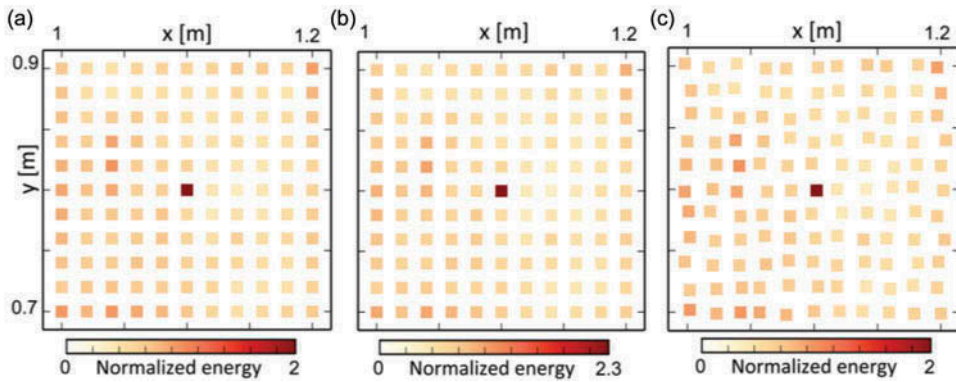


Figure 25. (a) The value of the energy $E(x, y)$ for the configuration in Figure 24 (c). (b) Same as (a), but for the configuration in Figure 24 (d). (c) Same as (a), but using a spatially random arrangement. Taken from Colombi *et al.* [58].

5. Conclusions

Microstructure designs of plate-type EMMs open an exciting avenue for applying metamaterial concept into real-world engineering applications. In this paper, different microstructural designs of LR-based EMM plates are reviewed. Some abnormal wave phenomenon caused by the metamaterial plates are demonstrated such as attenuation of low-frequency guided wave, subwavelength negative refraction, and energy trapping, and their potential applications are also summarized in vibration/noise isolation and SHM.

Disclosure statement

No potential conflict of interest was reported by the author(s).

Funding

This work was supported by the Air Force Office of Scientific Research [grant no. AF 9550-15-1-0061] with Program Manager Dr. Byung-Lip (Les) Lee. XN and GK are grateful to the National Natural Science Foundation of China [grants no. 11221202, 11290153, 11372035].

References

- [1] J.B. Pendry, A.J. Holden, D.J. Robbins, and W.J. Stewart, *Magnetism from conductors and enhanced nonlinear phenomena*, IEEE Trans. Microwave Theory Tech. 47 (1999), pp. 2075–2084. doi:10.1109/22.798002.
- [2] D.R. Smith, J.B. Pendry, and M.C.K. Wiltshire, *Metamaterials and negative refractive index*, Science 305 (2004), pp. 788–792. doi:10.1126/science.1096796.
- [3] S.H. Lee, C.M. Park, Y.M. Seo, Z.G. Wang, and C.K. Kim, *Acoustic metamaterial with negative density*, Phys. Lett. A. 373 (2009), pp. 4464–4469. doi:10.1016/j.physleta.2009.10.013.
- [4] N. Fang, D. Xi, J. Xu, M. Ambati, W. Srituravanich, C. Sun, and X. Zhang, *Ultrasonic metamaterials with negative modulus*, Nature Mater. 5 (2006), pp. 452–456. doi:10.1038/nmat1644.
- [5] D. Torrent and J. Sánchez-Dehesa, *Anisotropic mass density by two-dimensional acoustic metamaterials*, New J. Phys. 10 (2008), pp. 023004. doi:10.1088/1367-2630/10/2/023004.

- [6] L. Zigoneanu, B.I. Popa, and S.A. Cummer, *Design and measurements of a broadband two-dimensional acoustic metamaterial with anisotropic effective mass density*, J. Appl. Phys. 109 (2011), pp. 054906.
- [7] C. Shen, J. Xu, N. Fang, and Y. Jing, *Anisotropic complementary acoustic metamaterial for cancelling out aberrating layers*, Phys. Rev. X. 4 (2014), pp. 041033.
- [8] M. Kadic, T. Bückmann, R. Schittny, and M. Wegener, *Metamaterials beyond electromagnetism*, Rep. Prog. Phys. 76 (2013), pp. 126501. doi:10.1088/0034-4885/76/12/126501.
- [9] D. Bigoni, S. Guenneau, A.B. Movchan, and M. Brun, *Elastic metamaterials with inertial locally resonant structures: Application to lensing and localization*, Phys. Rev. B. 87 (2013), pp. 174303. doi:10.1103/PhysRevB.87.174303.
- [10] F. Bongard, H. Lissek, and J.R. Mosig, *Acoustic transmission line metamaterial with negative/zero/positive refractive index*, Phys. Rev. B. 82 (2010), pp. 094306. doi:10.1103/PhysRevB.82.094306.
- [11] M. Farhat, S. Guenneau, and S. Enoch, *Ultrabroadband elastic cloaking in thin plates*, Phys. Rev. Lett. 103 (2009), pp. 024301. doi:10.1103/PhysRevLett.103.024301.
- [12] J.H. Oh, H.M. Seung, and Y.Y. Kim, *A truly hyperbolic elastic metamaterial lens*, Appl. Phys. Lett. 104 (2014), pp. 073503. doi:10.1063/1.4865907.
- [13] Z.Y. Liu, X.X. Zhang, Y. Mao, Y.Y. Zhu, Z. Yang, C.T. Chan, and P. Sheng, *Locally resonant sonic materials*, Science 289 (2000), pp. 1734–1736. doi:10.1126/science.289.5485.1734.
- [14] G.W. Milton and J.R. Willis, *On modifications of Newton's second law and linear continuum elastodynamics*, Proc. Roy. Soc. A. 463 (2007), pp. 855–880. doi:10.1098/rspa.2006.1795.
- [15] S.S. Yao, X.M. Zhou, and G.K. Hu, *Experimental study on negative effective mass in a 1D mass–spring system*, New J. Phys. 10 (2008), pp. 043020. doi:10.1088/1367-2630/10/4/043020.
- [16] G. Wang, D. Yu, J. Wen, Y. Liu, and X. Wen, *One-dimensional phononic crystals with locally resonant structures*, Phys. Lett. A. 327 (2004), pp. 512–521. doi:10.1016/j.physleta.2004.05.047.
- [17] R. Zhu, G.L. Huang, and G.K. Hu, *Effective dynamic properties and multi-resonant design of acoustic metamaterials*, ASME J. Vib. Acoust. 134 (2012), pp. 031006. doi:10.1115/1.4005825.
- [18] S.S. Yao, X.M. Zhou, and G.K. Hu, *Investigation of the negative-mass behaviors occurring below a cut-off frequency*, New J. Phys. 12 (2010), pp. 103025. doi:10.1088/1367-2630/12/10/103025.
- [19] X.N. Liu, G.K. Hu, C.T. Sun, and G.L. Huang, *Wave propagation characterization and design of two-dimensional elastic chiral metacomposite*, J. Sound Vib. 330 (2011), pp. 2536–2553. doi:10.1016/j.jsv.2010.12.014.
- [20] Y.Y. Chen, G.L. Huang, and C.T. Sun, *Band gap control in an active elastic metamaterial with negative capacitance piezoelectric shunting*, ASME J. Vib. Acoust. 136 (2014), pp. 061008. doi:10.1115/1.4028378.
- [21] H.H. Huang and C.T. Sun, *Locally resonant acoustic metamaterials with 2D anisotropic effective mass density*, Philos. Mag. 91 (2011), pp. 981–996. doi:10.1080/14786435.2010.536174.
- [22] R. Zhu, H.H. Huang, G.L. Huang, and C.T. Sun, *Microstructure continuum modeling of an elastic metamaterial*, Int. J. Eng. Sci. 49 (2011), pp. 1477–1485. doi:10.1016/j.ijengsci.2011.04.005.
- [23] A.P. Liu, R. Zhu, X.N. Liu, G.K. Hu, and G.L. Huang, *Multi-displacement microstructure continuum modeling of anisotropic elastic metamaterials*, Wave Motion 49 (2012), pp. 411–426. doi:10.1016/j.wavemoti.2011.12.006.
- [24] G. Milton, *The Theory of Composites*, Cambridge University Press, Cambridge, 2002.
- [25] M. Kadic, T. Bückmann, N. Stenger, M. Thiel, and M. Wegener, *On the practicability of pentamode mechanical metamaterials*, Appl. Phys. Lett. 100 (2012), pp. 191901. doi:10.1063/1.4709436.
- [26] M. Kadic, T. Bückmann, R. Schittny, P. Gumbsch, and M. Wegener, *Pentamode metamaterials with independently tailored bulk modulus and mass density*, Phys. Rev. Appl. 2 (2014), pp. 054007.
- [27] T. Bückmann, R. Schittny, M. Thiel, M. Kadic, G.W. Milton, and M. Wegener, *On three-dimensional dilational elastic metamaterials*, New J. Phys. 16 (2014), pp. 033032. doi:10.1088/1367-2630/16/3/033032.

- [28] J.O. Vasseur, P.A. Deymier, B. Djafari-Rouhani, Y. Pennec, and A.-C. Hladky-Hennion, *Absolute forbidden bands and waveguiding in two-dimensional phononic crystal plates*, Phys. Rev. B. 77 (2008), pp. 085415. doi:10.1103/PhysRevB.77.085415.
- [29] F. Hsiao, A. Khelif, H. Moubchir, A. Choujaa, C. Chen, and V. Laude, *Waveguiding inside the complete band gap of a phononic crystal slab*, Phys. Rev. E. 76 (2007), pp. 056601. doi:10.1103/PhysRevE.76.056601.
- [30] R. Zhu, G.L. Huang, H.H. Huang, and C.T. Sun, *Experimental and numerical study of guided wave propagation in a thin metamaterial plate*, Phys. Lett. A. 375 (2011), pp. 2863–2867. doi:10.1016/j.physleta.2011.06.006.
- [31] C.-Y. Sun, J.-C. Hsu, and T.-T. Wu, *Resonant slow modes in phononic crystal plates with periodic membranes*, Appl. Phys. Lett. 97 (2010), pp. 031902. doi:10.1063/1.3464955.
- [32] R. Zhu, X.N. Liu, G.K. Hu, C.T. Sun, and G.L. Huang, *Negative refraction of elastic waves at the deep subwavelength scale in a single-phase metamaterial*, Nature Commun. 5 (2014), pp. 5510. doi:10.1038/ncomms6510.
- [33] T.-T. Wu, Z.-G. Huang, T.-C. Tsai, and T.-C. Wu, *Evidence of complete band gap and resonances in a plate with periodic stubbed surface*, Appl. Phys. Lett. 93 (2008), pp. 111902. doi:10.1063/1.2970992.
- [34] M. Oudich, Y. Li, B.M. Assouar, and Z.L. Hou, *A sonic band gap based on the locally resonant phononic plates with stubs*, New J. Phys. 12 (2010), pp. 083049. doi:10.1088/1367-2630/12/8/083049.
- [35] J.-C. Hsu, *Local resonances-induced low-frequency band gaps in two-dimensional phononic crystal slabs with periodic stepped resonators*, J. Phys. D: Appl. Phys. 44 (2011), pp. 055401. doi:10.1088/0022-3727/44/5/055401.
- [36] J.-C. Hsu and T.-T. Wu, *Lamb waves in binary locally resonant phononic plates with two-dimensional lattices*, Appl. Phys. Lett. 90 (2007), pp. 201904. doi:10.1063/1.2739369.
- [37] R. Zhu, X.N. Liu, G.L. Huang, H.H. Huang, and C.T. Sun, *Microstructural design and experimental validation of elastic metamaterial plates with anisotropic mass density*, Phys. Rev. B. 86 (2012), pp. 144307. doi:10.1103/PhysRevB.86.144307.
- [38] H.H. Huang, C.T. Sun, and G.L. Huang, *On the negative effective mass density in acoustic metamaterials*, Int. J. Eng. Sci. 47 (2009), pp. 610–617. doi:10.1016/j.jengsci.2008.12.007.
- [39] R. Marchal, O. Boyko, B. Bonello, J. Zhao, L. Belliard, M. Oudich, Y. Pennec, and B. Djafari-Rouhani, *Dynamics of confined cavity modes in a phononic crystal slab investigated by in situ time-resolved experiments*, Phys. Rev. B. 86 (2012), pp. 224302. doi:10.1103/PhysRevB.86.224302.
- [40] A. Khelif, B. Aoubiza, S. Mohammadi, A. Adibi, and V. Laude, *Complete band gaps in two-dimensional phononic crystal slabs*, Phys. Rev. E. 74 (2006), pp. 046610. doi:10.1103/PhysRevE.74.046610.
- [41] X.N. Liu, G.L. Huang, and G.K. Hu, *Chiral effect in plane isotropic micropolar elasticity and its application to chiral lattices*, J. Mech. Phys. Solids. 60 (2012), pp. 1907–1921. doi:10.1016/j.jmps.2012.06.008.
- [42] T.T. Wu and Z.G. Huang, *Level repulsions of bulk acoustic waves in composite materials*, Phys. Rev. B. 70 (2004), pp. 214304.
- [43] G. Wang, X. Wen, J. Wen, L. Shao, and Y. Liu, *Two-dimensional locally resonant phononic crystals with binary structures*, Phys. Rev. Lett. 93 (2004), pp. 154302. doi:10.1103/PhysRevLett.93.154302.
- [44] M.S. Kushwaha, P. Halevi, L. Dobrzynski, and B. Djafari-Rouhani, *Acoustic band structure of periodic elastic composites*, Phys. Rev. Lett. 71 (1993), pp. 2022–2025. doi:10.1103/PhysRevLett.71.2022.
- [45] J.-C. Hsu and T.-T. Wu, *Efficient formulation for band-structure calculations of two-dimensional phononic-crystal plates*, Phys. Rev. B. 74 (2006), pp. 144303. doi:10.1103/PhysRevB.74.144303.
- [46] C. Goffaux and J. Sánchez-Dehesa, *Two-dimensional phononic crystals studied using a variational method: Application to lattices of locally resonant materials*, Phys. Rev. B. 67 (2003), pp. 144301. doi:10.1103/PhysRevB.67.144301.
- [47] L. Fok, M. Ambati, and X. Zhang, *Acoustic metamaterials*, MRS Bull. 33 (2008), pp. 931–934. doi:10.1557/mrs2008.202.

- [48] X.N. Liu, G.K. Hu, G.L. Huang, and C.T. Sun, *An elastic metamaterial with simultaneously negative mass density and bulk modulus*, Appl. Phys. Lett. 98 (2011), pp. 251907. doi:[10.1063/1.3597651](https://doi.org/10.1063/1.3597651).
- [49] M. Oudich, M.B. Assouar, and Z.L. Hou, *Propagation of acoustic waves and waveguiding in a two-dimensional locally resonant phononic crystal plate*, Appl. Phys. Lett. 97 (2010), pp. 193503. doi:[10.1063/1.3513218](https://doi.org/10.1063/1.3513218).
- [50] T.-T. Wu, Y.-T. Chen, J.-H. Sun, S.C.S. Lin, and T.J. Huang, *Focusing of the lowest antisymmetric Lamb wave in a gradient-index phononic crystal plate*, Appl. Phys. Lett. 98 (2011), pp. 171911. doi:[10.1063/1.3583660](https://doi.org/10.1063/1.3583660).
- [51] J.F. Zhao, R. Marchal, B. Bonello, and O. Boyko, *Efficient focalization of antisymmetric Lamb waves in gradient-index phononic crystal plates*, Appl. Phys. Lett. 101 (2012), pp. 261905. doi:[10.1063/1.4773369](https://doi.org/10.1063/1.4773369).
- [52] S.-C. Lin, T.J. Huang, J.-H. Sun, and T.-T. Wu, *Gradient-index phononic crystals*, Phys. Rev. B. 79 (2009), pp. 094302. doi:[10.1103/PhysRevB.79.094302](https://doi.org/10.1103/PhysRevB.79.094302).
- [53] X. Yan, R. Zhu, G.L. Huang, and F.-G. Yuan, *Focusing guided waves using surface bonded elastic metamaterials*, Appl. Phys. Lett. 103 (2013), pp. 121901. doi:[10.1063/1.4821258](https://doi.org/10.1063/1.4821258).
- [54] J.B. Pendry, *Negative refraction makes a perfect lens*, Phys. Rev. Lett. 85 (2000), pp. 3966–3969. doi:[10.1103/PhysRevLett.85.3966](https://doi.org/10.1103/PhysRevLett.85.3966).
- [55] R.A. Shelby, D.R. Smith, and S. Schultz, *Experimental verification of a negative index of refraction*, Science 292 (2001), pp. 77–79. doi:[10.1126/science.1058847](https://doi.org/10.1126/science.1058847).
- [56] J.-F. Robillard, J. Bucay, P.A. Deymier, A. Shelke, K. Muralidharan, B. Merheb, J.O. Vasseur, A. Sukhovich, and J.H. Page, *Resolution limit of a phononic crystal superlens*, Phys. Rev. B. 83 (2011), pp. 224301. doi:[10.1103/PhysRevB.83.224301](https://doi.org/10.1103/PhysRevB.83.224301).
- [57] S. Zhang, L.L. Yin, and N. Fang, *Focusing ultrasound with an acoustic metamaterial network*, Phys. Rev. Lett. 102 (2009), pp. 194301. doi:[10.1103/PhysRevLett.102.194301](https://doi.org/10.1103/PhysRevLett.102.194301).
- [58] A. Colombi, P. Roux, and M. Rupin, *Sub-wavelength energy trapping of elastic waves in a metamaterial*, J. Acoust. Soc. Am. 136 (2014), pp. EL192–EL198. doi:[10.1121/1.4890942](https://doi.org/10.1121/1.4890942).